Supplemental Material for

Fourier optical spin splitting microscopy

Junxiao Zhou[1+], Qianyi Wu[1+], Junxiang Zhao[1+], Clara Posner[2], Ming Lei[1], Guanghao Chen[1], Zhang Jin[2], Zhaowei Liu[1]*

[1]*Department of Electrical and Computer Engineering, University of California, San Diego, 9500 Gilman Drive, La Jolla, California 92093, United States*

[2]*Department of Pharmacology, University of California, San Diego, La Jolla, California 92093, United States*

* *Zhaowei Liu* zhaowei@ucsd.edu

These authors contributed equally to this work

This file includes:

1. Metasurface fabrication

Laser writing on bulk SiO_2 substrate provides the birefringence required by the geometric phase metasurface. Under intense laser irradiation, several tens of randomly distributed nanopores are created near the laser focal spots within a volume of bulk SiO_2, wherein each individual nanopore has an elongated oblate cross section in a plane parallel to the surface of the metasurface. The elongated shape of the nanopores is responsible for the induced birefringence. The long axis of the randomly distributed nanopores (the direction of the slow axis direction of the induced birefringence) is perpendicular to the polarization of the writing laser beam. The key parameter for birefringent operation is the phase retardance, defined as the optical delay between the fast and slow polarization axes. The phase retardation of the patterned volume $\vartheta = 2\pi(n_{xx} - n_{yy})h / \lambda$ is determined by the refractive index contrast $n_{xx} - n_{yy}$ and the writing depth h. Here, n_{xx} and n_{yy} are the local effective refractive indices of the patterned volume along the nanopores short axis and long axis and are related to the filling factor of nanopores in SiO_2 as well as the host material refractive index. In a geometric phase system, ϑ should be equal to π to maximize the phase modulation efficiency. To manipulate the local wavefront of the incident light, we change the orientation of the nanopores in the local volume by controlling the polarization of the incident writing laser.

In our experiment, we fabricated a metasurface with an area of 6 mm*6 mm inside a SiO_2 substrate with a diameter of 2.54 cm. The writing laser is a PHAROS Yb-doped potassium gadolinium tungstate-based mode-lock regenerative amplified Yb:KGW (Ytterbium-doped potassium gadolinium tungstate) based femtosecond laser system (Pharos, Light Conversion Ltd.) working at 1030 nm wavelength (photon energy ~ 1.2 eV). The laser has a variable repetition rates (Viosil, ShinEtsu, OH content 1200 ppm) from 1kHz to 1MHz and a pulse duration is from 190 fs to 10 ps. The laser beam is focused into a 3 mm thick bulk SiO_2 with ~5 μm in diameter at the focal point by a 0.16 numerical aperture aspheric objective lens. The SiO_2 sample was mounted onto XYZ computer-controlled three-axial air-bearing translation stage (Aerotech Ltd.). The polarization is rotated by an electro-optic modulator. If more than one layer of nanostructures is to be imprinted into the metasurface, scanning along the scan path can be repeated at other depths within the sample thickness by changing the position of the sample relative to the focusing arrangement along the beam propagation direction. Alternatively, the focusing depth might be altered during a scan to form nanostructures at varying depths.

The fabricated metasurface nanostructure is embedded in the glass substrate at ~0.65 mm from the top surface. The total thickness of the nanostructure layer is ~1 mm. Due to the weak birefringence $\left(n_{xx} - n_{yy} \approx 5\times10^{-4}\right)$, 25 birefringent layers were fabricated with a layer separation of ~40 μm. Note that the nonnegligible thickness of the metasurface requires the 4*f* system with reasonable focal length so that paraxial approximation can be applied properly. The transmission of the metasurface is related to the size

of the nanopores, which is determined by the laser pulse density. To achieve higher transmission efficiency, the size of the nanopores should be small enough to reduce the Rayleigh scattering. The lengths and widths of the elongated nanopores in our samples are typically around 40 nm and 20 nm, respectively. The total transmission is $>$ 95% at the working wavelength.

Figure S1(a) shows the crossed polarization image of the sample. Each two pairs of transmitting stripes correspond to one metasurface period based on the transmittance profile described by $t_{ms}(x,y)=\sin(2\pi x/\Lambda)$. The slow axis orientation distribution of the metasurface is shown in Fig. S1(b). The spatially distributed angle from -90° to 90° indicates the final geometric phase of the metasurface ranging from -180° to 180°. Fig. S1(c) presents the polarized microscope transmittance image of the boxed region of the metasurface in Fig. S1(a). Figure S1(d) shows the effective optical axis distribution of the boxed region of the metasurface in Fig. S1(b). A scanning electron microscope image of the laser written area shows the formation of the nanopore defects within the metasurface. The black elongated nanopores has the smallest feature size of ~20 nm.

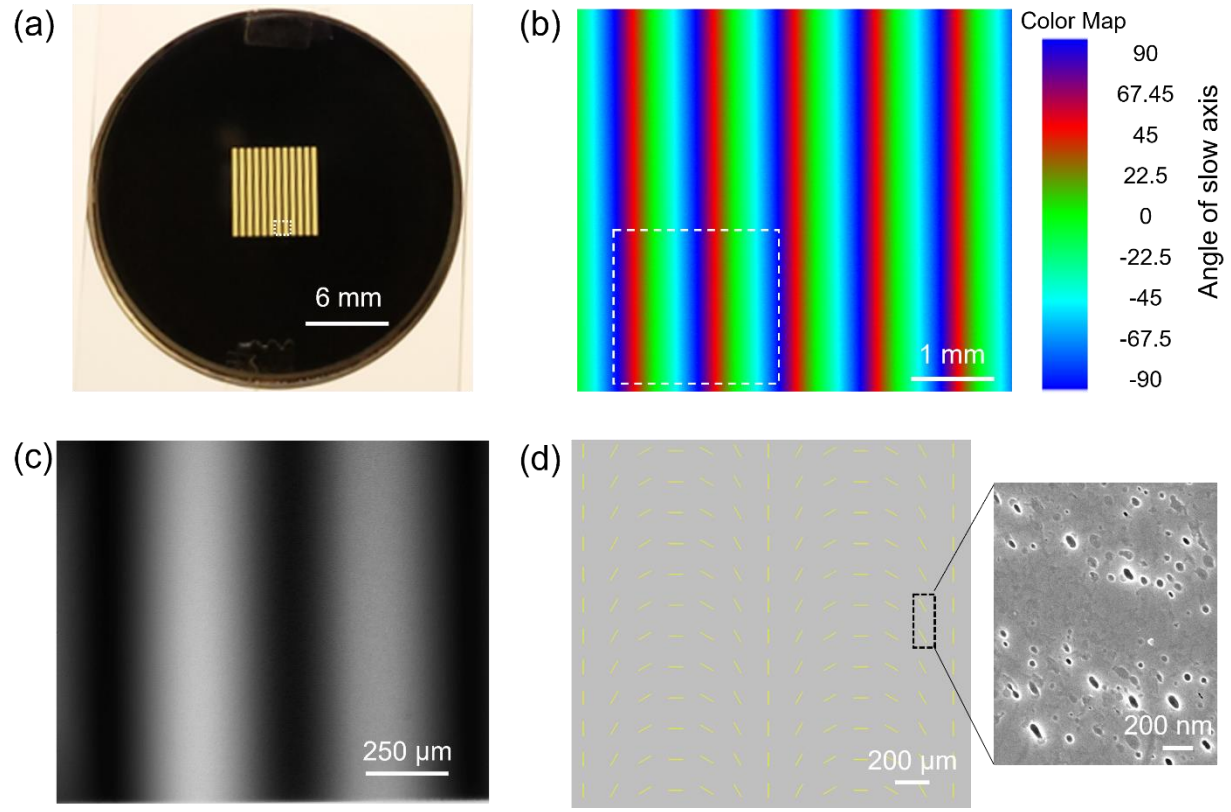

FIG. S1 The metasurface information. (a) Crossed polarization image. (b) Slow axis distribution. (c) Zoomed in area in (a), which is taken by a microscope. (d) The effective optical axis distribution. The right panel is the scanning electron microscope image of the sample area.

2. Theory of tunable retardance imaging

Geometric phase results from polarization change and the local orientation of the optical axis of the metasurface. The Jones matrix of the designed geometric phase metasurface with constant phase retardance π and spatially varying local optical axes φ is given as:

$$T_0 = \begin{bmatrix} \cos 2\varphi & \sin 2\varphi \\ \sin 2\varphi & -\cos 2\varphi \end{bmatrix} \tag{S1}$$

Here, $\varphi(x,y) = \pi x/\Lambda$, assuming the phase gradient direction is along x axis. Given the metasurface is sandwiched between two orthogonal linear polarizer (x-polarized) and analyzer (y-polarized), the Jones matrix of the combination of the three components can be written as

$$T_{\text{eff}} = P_2 T_0 P_1 = \begin{bmatrix} 0 & 0 \\ 0 & 1 \end{bmatrix} \begin{bmatrix} \cos 2\varphi & \sin 2\varphi \\ \sin 2\varphi & -\cos 2\varphi \end{bmatrix} \begin{bmatrix} 1 & 0 \\ 0 & 0 \end{bmatrix} = \begin{bmatrix} 0 & 0 \\ \sin 2\varphi & 0 \end{bmatrix} \tag{S2}$$

which shows the combined device can be understood as an effective amplitude grating which changes the polarization of the input light by 90 degrees and exhibits a sinusoidal transmittance function $t_{ms}(x,y) = \sin(2\pi x/\Lambda)$.

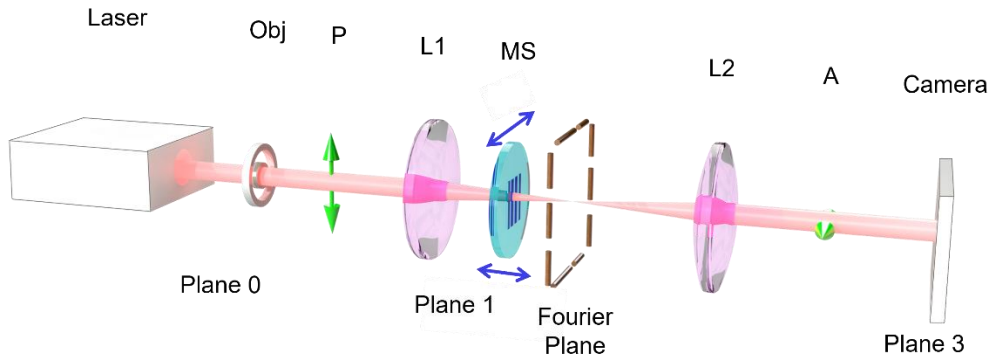

FIG. S2. Measurement setup. L1 and L2, lens. P, polarizer. A, analyzer. MS, metasurface. Fourier plane, Plane 2.

To illustrate the formation of image when the metasurface is placed with a transverse shift s along x axis and a longitudinal shift ε along z axis with respect to the origin of the Fourier plane (FP), we apply the scalar diffraction with the angular spectrum method of analysis. Figure S2 shows the experiment setup. Denote the electrical field of the input object at Plane 0 as $E_{in}(x_0, y_0)$. The angular spectrum of the electric field $E_2(x_2, y_2)$ on FP is $F_2(f_x, f_y) = F\,[E_2(x_2, y_2)]$, where F is the Fourier-transform operator. Under Fresnel approximation, $F_1(f_x, f_y)$ on Plane 1 which is $|\varepsilon|(\varepsilon < 0)$ in front of the FP is related to the angular spectrum $F_2(f_x, f_y)$ by

$$F_2(f_x, f_y) = F_1(f_x, f_y)\exp[\mathrm{j}\pi\lambda\varepsilon(f_x^2 + f_y^2)] \tag{S3}$$

Thus, with Eq. S3 and consider $E_2(x_2, y_2)$ will be the Fourier transform of the input object in the absence

of metasurface, the angular spectrum on Plane 1 can be determined by

$$F_1(f_x, f_y) = E_{in}(-\lambda f_1 f_x, -\lambda f_1 f_y)\exp[-\mathrm{j}\pi\lambda\varepsilon(f_x^2 + f_y^2)] \tag{S4}$$

where f_1 (f_2) is the focal distance of L1 (L2). With metasurface placed on Plane 1, the angular spectrum just behind the metasurface is the convolution of $F_1(f_x, f_y)$ and the Fourier transform of the transmittance function $t_{ms}(x_1 - s, y_1)$ of metasurface, which can be expressed by

$$\begin{aligned}
\mathrm{F}_1'(f_x, f_y) &= \left\{E_{in}(-\lambda f_1 f_x, -\lambda f_1 f_y)\exp[-\mathrm{j}\pi\lambda\varepsilon(f_x^2 + f_y^2)]\right\} * \left\{-\frac{j}{2}\left[\exp(-\mathrm{j}\theta)\delta\left(f_x - \frac{1}{\Lambda}\right) - \exp(\mathrm{j}\theta)\delta\left(f_x + \frac{1}{\Lambda}\right)\right]\right\} \\
&= -\frac{j}{2}E_{in}\left[-\lambda f_1 f_x + \frac{\lambda f_1}{\Lambda}, -\lambda f_1 f_y\right]\exp\left\{-\mathrm{j}\theta - \mathrm{j}\pi\lambda\varepsilon\left[\left(f_x - \frac{1}{\Lambda}\right)^2 + f_y^2\right]\right\} \\
&\quad + \frac{j}{2}E_{in}\left[-\lambda f_1 f_x - \frac{\lambda f_1}{\Lambda}, -\lambda f_1 f_y\right]\exp\left\{\mathrm{j}\theta - \mathrm{j}\pi\lambda\varepsilon\left[\left(f_x + \frac{1}{\Lambda}\right)^2 + f_y^2\right]\right\}
\end{aligned} \tag{S5}$$

where $*$ is the convolution operator, $\theta = 2\pi s / \Lambda$.

With Fresnel propagation, the angular spectrum on the FP is given by

$$F_2(f_x, f_y) = -\frac{j}{2}\exp\left(-j\pi\frac{\lambda\varepsilon}{\Lambda^2}\right)\left[E_{in}\left(-\lambda f_1 f_x + \frac{\lambda f_1}{\Lambda}, -\lambda f_1 f_y\right)\exp\left(\mathrm{j}2\pi\frac{\lambda\varepsilon}{\Lambda}f_x - \mathrm{j}\theta\right) - E_{in}\left(-\lambda f_1 f_x - \frac{\lambda f_1}{\Lambda}, -\lambda f_1 f_y\right)\exp\left(-\mathrm{j}2\pi\frac{\lambda\varepsilon}{\Lambda}f_x + \mathrm{j}\theta\right)\right] \tag{S6}$$

To understand the functionality of metasurface, the electric field on the FP is calculated with the inverse Fourier transform as

$$E_2'(x_2, y_2) = -\frac{j}{2}\exp\left(-j\pi\frac{\lambda\varepsilon}{\Lambda^2}\right)\left[E_2^{(0)}(x_2, y_2)\exp\left(j\frac{2\pi}{\Lambda}x_2 - j\theta\right) * \delta\left(x_2 + \frac{\lambda\varepsilon}{\Lambda}\right) - E_2^{(0)}(x_2, y_2)\exp\left(-j\frac{2\pi}{\Lambda}x_2 + j\theta\right) * \delta\left(x_2 - \frac{\lambda\varepsilon}{\Lambda}\right)\right] \tag{S7}$$

where $E_2^{(0)}(x_2, y_2)$ is the electric field on FP without the metasurface in the setup. This result shows effectively, the electric field on the FP simultaneously experienced an angular shift and a spatial shift induced by the metasurface. A similar derivation for the case when metasurface is placed behind the FP $(\varepsilon > 0)$ yields the same expression for $E_2'(x_2, y_2)$ as Eq. S7.

The output electric field on the image plane turns out to be the subtraction of two laterally sheared images with different phase retardation, which is written as

$$\begin{aligned}
\mathrm{E}_3(x_3, y_3) &= F\ [\mathrm{E}_2(x_2, y_2)]|_{f_x = \frac{x_3}{\lambda f_2}, f_y = \frac{y_3}{\lambda f_2}} = F_2\left(\frac{x_3}{\lambda f_2}, \frac{y_3}{\lambda f_2}\right) \\
&= -\frac{j}{2}\exp\left(-j\pi\frac{\lambda\varepsilon}{\Lambda^2}\right)\left\{E_{in}\left(\frac{x_3 - \Delta}{M}, \frac{y_3}{M}\right)\exp[j\beta(x_3) - j\theta] - E_{in}\left(\frac{x_3 + \Delta}{M}, \frac{y_3}{M}\right)\exp[-j\beta(x_3) + j\theta]\right\}
\end{aligned} \tag{S8}$$

where $2\Delta = 2\lambda f_2 / \Lambda$ is the shearing distance, $M = -f_2 / f_1$ is the magnification, $\beta(x_3) = \pm 2\pi\varepsilon x_3 / (\Lambda f_2)$ is a spatially varying phase resulted from the longitudinal shift ϵ of metasurface, $\theta = 2\pi s / \Lambda$ represents a bias phase brought by the transverse shift s of metasurface.

For simplicity, consider the case when $f_1 = f_2$ and flip the coordinate of the image plane. With a phase object $E_{in}(x_0, y_0) = \mathrm{A}\exp[\mathrm{j}\phi(x_0, y_0)]$, the intensity to be captured at the image plane is given by

$$\begin{aligned} I_{out}(x_3, y_3) &= \frac{1}{4}\left|E_{in}(x_3 + \Delta, y_3)\exp[-\mathrm{j}\beta(x_3) - \mathrm{j}\theta] - E_{in}(x_3 - \Delta, y_3)\exp[\mathrm{j}\beta(x_3) + \mathrm{j}\theta]\right|^2 \\ &= \frac{A^2}{4}\left|\exp[-\mathrm{j}\beta(x_3) - \mathrm{j}\theta]\exp[-\mathrm{j}\phi(x_3 - \Delta, y_3)] - \exp[\mathrm{j}\beta(x_3) + \mathrm{j}\theta]\exp[\mathrm{j}\phi(x_3 + \Delta, y_3)]\right|^2 \quad \text{(S9)} \\ &= \frac{A^2}{2}\{1 - \cos[\phi(x_3 + \Delta, y_3) - \phi(x_3 - \Delta, y_3) - 2\beta(x_3) - 2\theta]\} \end{aligned}$$

The image contrast varies as the bias retardation between the LCP and RCP changes. Assume the object has unity amplitude, i.e., A=1 and consider the metasurface located at the Fourier plane, i.e., $\beta(x_3) = 0$. For simplicity, we define the phase gradient of the object as $\Phi = \phi(x_3 + \Delta, y_3) - \phi(x_3 - \Delta, y_3)$. The signal could be given as: $I_{\text{signal}} = \frac{1}{2}[1 - \cos(\Phi - 2\theta)]$. The background could be written as: $I_{bg} = \frac{1}{2}[1 - \cos(-2\theta)]$. Therefore, the image contrast could be given as

$$\begin{aligned} C &= \left|\frac{I_{\text{signal}} - I_{bg}}{I_{bg}}\right| = \left|\frac{-\cos 2\theta \cos\Phi - \sin 2\theta \sin\Phi + \cos 2\theta}{1 - \cos 2\theta}\right| \\ &= \left|\frac{1}{2}(1 - \cos\Phi)\left(\cot\theta - \frac{\sin\Phi}{1 - \cos\Phi}\right)^2 - 1\right| \end{aligned} \quad \text{(S10)}$$

As we can tell the cotangent term dominates the overall image contrast. When the bias retardation 2θ approaches 0 or 2π, the two replicas interfere destructively, and the background goes to almost zero resulting in maximum image contrast.

3. Retardance images of polystyrene beads

To validate the tenability of the bias retardation in FOSSM, we image sparsely distributed polystyrene beads of 1 μm in diameter (Polybead, Polysciences, Warrington, PA, USA) with the metasurface placed in the center of the back aperture plane, which corresponds to $\varepsilon = 0$ in Eq. 2. A fiber coupled 532 nm continuous wave laser is used for illumination. When the metasurface is translated along its phase gradient direction, retardance images with intensity corresponding to the positive and negative phase gradients of the symmetric microspheres are captured as shown in Fig. S3(a)-(e). Note that the imaging system is designed such that the shear distance (~1.5 μm) is larger than the size of the microsphere; therefore, two isolated images of the same microsphere with bias retardation determined by the metasurface position are captured in each shot. The cross sections along the white dashed lines are shown in Fig. S3(f)-(j).

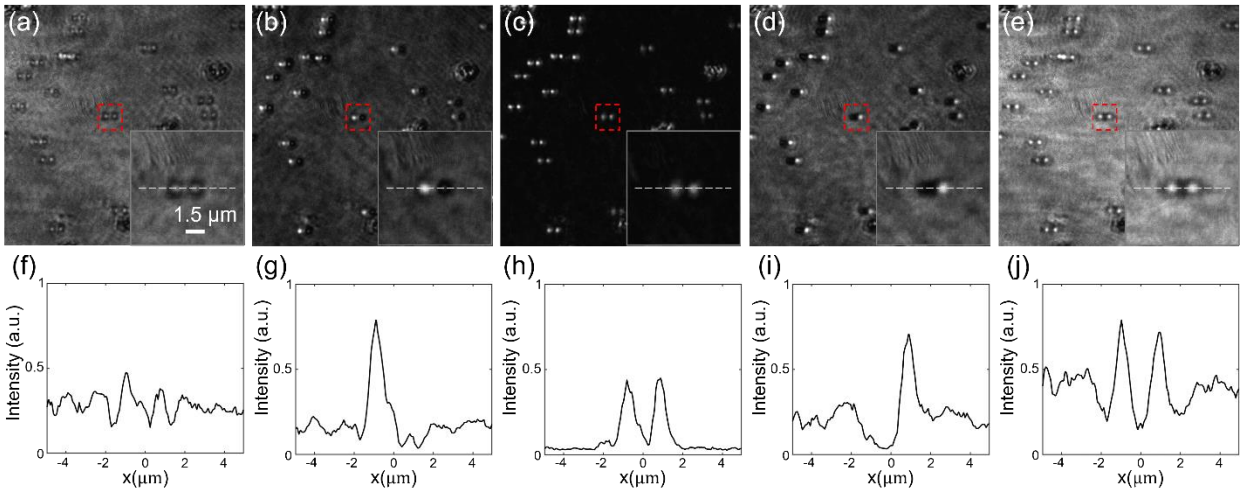

FIG. S3 (a)-(e) Retardance images of the polystyrene beads with retardation bias of $-\pi$, $-\pi/2$, 0, $\pi/2$, π. Insets, zoomed-in images of the regions in the red dashed box. (f)-(j) the cross sections along the white dashed lines in the inset in (a)-(e).

4. Cell preparation

HEK 293 cells were cultured in Dulbecco modified Eagle medium (DMEM; Gibco) containing 4.5 g/L glucose and supplemented with 10% (v/v) fetal bovine serum (FBS, Sigma) and 1% (v/v) penicillin-streptomycin (Pen-Strep, Sigma-Aldrich). NIH3T3 cells (CRL-1658, ATCC) were cultured in DMEM containing 1 g/L glucose supplemented with 10% calf serum (30-2030, ATCC) and 1% of penicillin-streptomycin (Sigma-Aldrich). Cells were maintained in a humidified incubator at 37°C with a 5% CO_2 atmosphere. For imaging, cells were grown overnight on top of glass coverslips placed in 6-well plates. Cells were then fixed with 4% paraformaldehyde in Phosphate-Buffered Saline (PBS) for 20 minutes at room temperature and then rinsed once with PBS after fixation. The glass coverslips containing cells were then mounted onto microscope slides using ProLong™ Glass Antifade Mountant with NucBlue™ Stain (ThermoFisher Scientific) and left to cure overnight at room temperature before imaging.

5. PMMA sample preparation

PMMA (Sigma-Aldrich) powder was dissolved in toluene with 30 mg/ml concentration. A glass coverslip was cleaned with acetone, isopropanol, and water in order. The PMMA solution was then spin-coated on the glass coverslip at 3000 rpm for 40 s. The coverslip covered with PMMA solution is then placed on a 200 °C hot plate for 7 min to anneal. The thickness step was created using O_2 plasma etching. Half of the PMMA film was protected by a layer of tape. Under 250W forward RF power for 5 minutes, the exposed PMMA film was totally etched off from the sample. The PMMA sample is then ready for imaging after peeling off the tape.

6. Phase retrieval algorithm

The phase information is retrieved in two steps. Firstly, the phase gradient with respect to x and y is calculated with a three-step phase shifting method. When the metasurface is limited to move within the FP, for each direction, three images with phare retardations of -120°, 0°, 120° are taken to calculate the phase gradients G_x and G_y in the main text. For the case when the metasurface is moving along the optical axis, three images with phare retardations around -120°, 0°, 120° in a certain area containing the targeted object are captured for both horizontal and vertical directions, respectively. Local phase retardations are estimated pixelwise by evaluating the sinusoidal background in the images and plugged into a generalized phase-stepping algorithm [1], which solves G_x and G_y in a least-squares manner. In the second step, the phase of the object is reconstructed with a least-squares integration method based on finite difference. According to Eq. S9, the phase gradients G_x and G_y are the difference between two pairs of horizontally and vertically sheared objects with a shearing distance 2Δ, respectively. Thus, the phase gradients can be represented by a matrix-vector multiplication [2]

$$g = A' p \tag{S11}$$

where $g = [\mathrm{vec}(G_x) \quad \mathrm{vec}(G_y)]^T$ is vectorized phase gradients, A' is the finite difference matrix considering the shearing distance 2Δ, p is the vectorized phase of the object.

To reconstruct the phase of the object, we apply a weighted l_2-norm total variation prior and solve the inverse problem

$$\hat{p} = \underset{p \in \mathbb{R}^{MN}}{\mathrm{argmin}} \left\| A' p - g \right\|_2 + \lambda \left\| W \cdot \nabla_{xy} p \right\|_2 \tag{S12}$$

where λ is the regularization parameter, W is a weighting matrix, $\cdot$ denotes element-wise multiplication, $\nabla_{xy} = \begin{bmatrix} \nabla_x & \nabla_y \end{bmatrix}^T$ is the matrix of forward finite differences in the x and y directions, MN is the number of pixels. To solve the problem in Eq. S12, we used CVX, a package for specifying and solving convex programs [3, 4].

Fig. S4 shows the simulated two sets of three retardance images when the metasurface is shifted along x and y axes and the phase retrieval process for a phase object with unity amplitude.

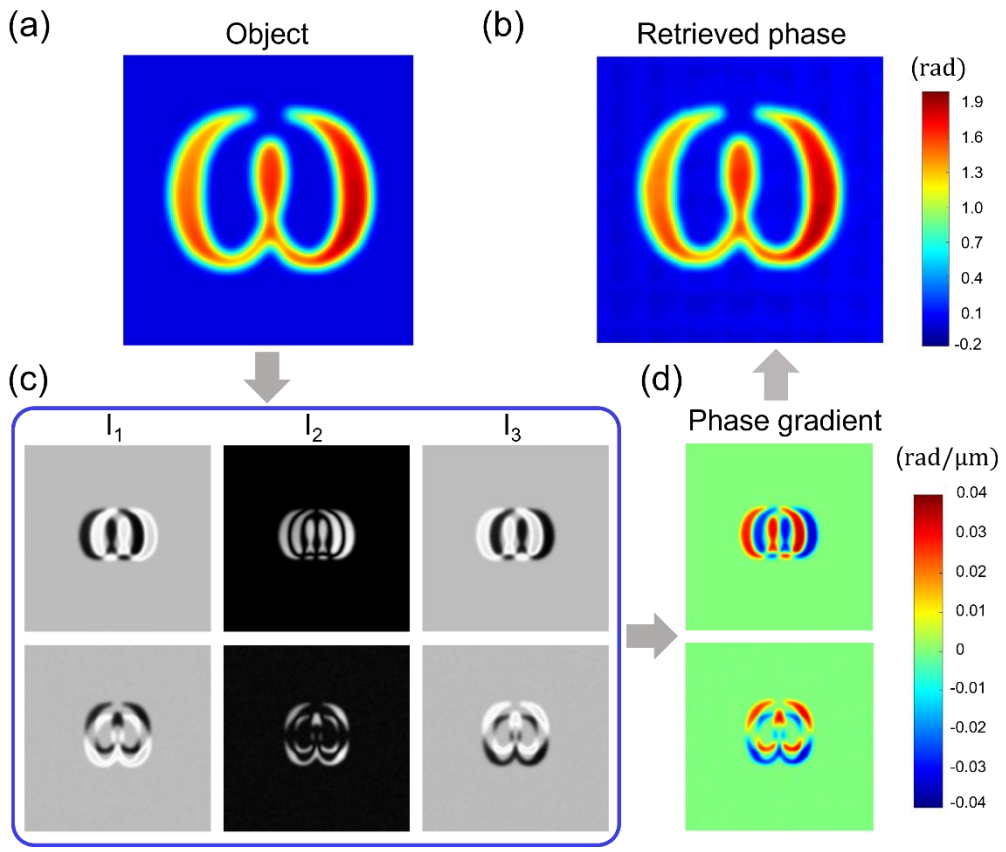

FIG. S4. Simulation of retardance images and phase retrieval when the metasurface is shifted within the FP. (a) The phase of the object. (b) The retrieved phase. (c) Three retardance images with phare delays of -120°, 0°, 120° for x and y directions, respectively. (d) The phase gradients with respect to x and y calculated from (c).

7. Retardance imaging of a water droplet with a longitudinally displaced metasurface

Fig. S5 shows the blending of retardance with continuously varying bias retardations as we move the metasurface away from the Fourier plane of the microscope. A phase object is imaged by FOSSM with the metasurface centered at the optical axis ($s=0$) at the Fourier plane. Different frames are captured when the metasurface is moved away from the Fourier plane along the optical axis while maintained centered in the x-y plane. When the metasurface is exactly at the Fourier plane ($s=0$, $\varepsilon=0$), the system performs regular edge detection imaging as shown in Fig. S5(b). As the metasurface moves along the z-axis in either direction, as shown in Fig. S5(c)-(h), the spatially varying phases of the two sheared replicas form a sinusoidal background over the imaging area, which indicates a spatially dependent phase retardation. Here in the images, the regions with bright peaks of the interference patterns correspond to zero phase retardation which leads to image addition, while the regions with dark valleys of the interference patterns correspond to a π phase retardation which leads to edge detection. The size of the edge detection imaging regions varies with respect to the distance ε between the metasurface and the Fourier plane according to Eq. 2.

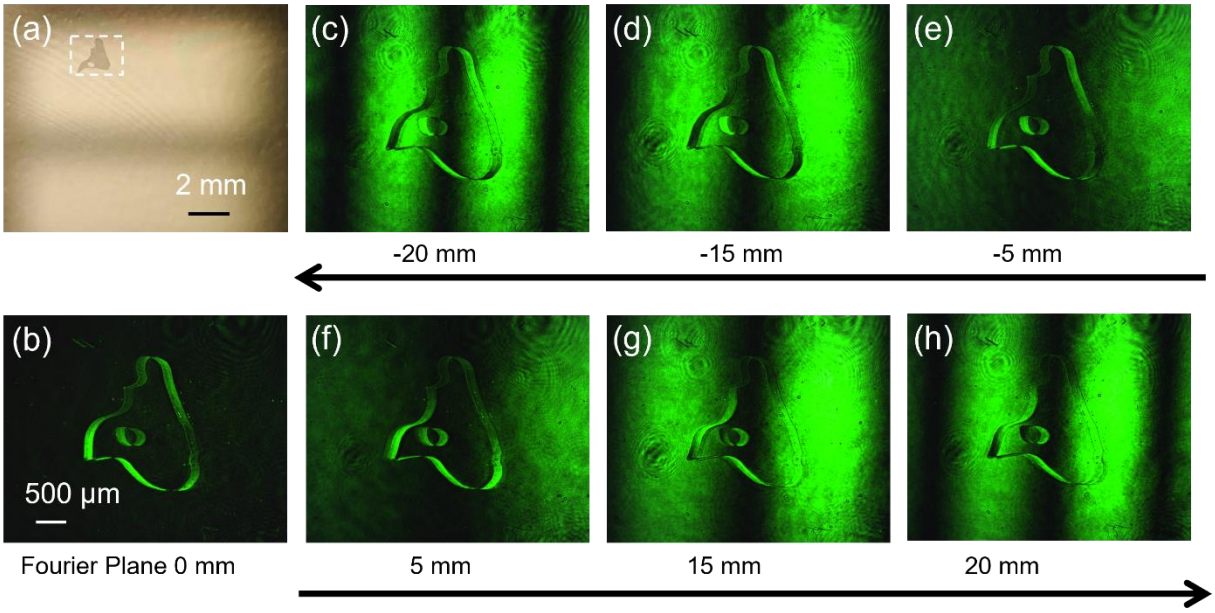

FIG. S5. Retardance imaging of a water droplet with a longitudinally displaced metasurface. (a) A small water droplet sandwiched between two glass coverslips is used as the phase object. (b) The edge-detection image of the object is formed using a 4*f* system with the metasurface placed symmetrically in the Fourier plane. (c)-(h) Images with the metasurface moved away from the Fourier plane by -20 mm, -15 mm, -5 mm, 0 mm, 5 mm, 15 mm, and 20 mm, respectively. The interference pattern becomes higher in spatial frequency as the metasurface is moved further away from the Fourier plane, indicating a faster varying phase retardation.

8. Quantitative phase imaging (QPI) of NIH3T3 cells with a longitudinally displaced metasurface

We further demonstrate the QPI capability when the metasurface is moved away from the Fourier plane. Within a neighborhood of the area of interest, the spatially varying phase $\exp[-\mathrm{j}\beta(x)]$ can be estimated pixelwise by analyzing the sinusoidal background. By translating the metasurface along the optical axis, three images with well separated phase retardations were taken to reconstruct the phase gradient image with the generalized phase-stepping algorithm. Figure S6(e) shows the retrieved QPI image of an NIH3T3 cell. Figure S6(j) shows the QPI image of the PMMA thin film sample with a thickness of 110 nm. The extracted phase matches with the film thickness.

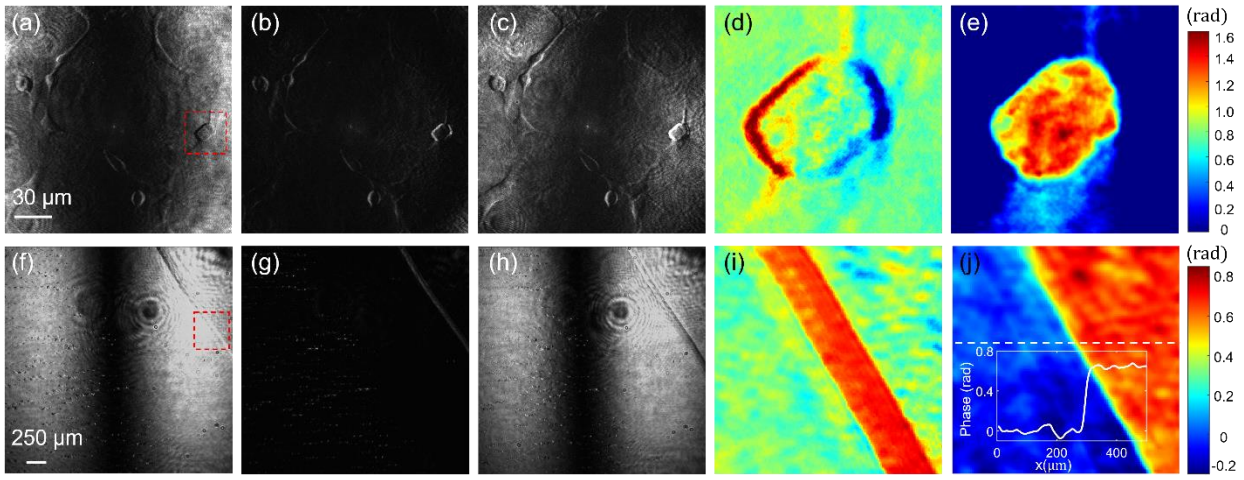

FIG. S6. QPI of NIH3T3 cells with a longitudinally displaced metasurface. (a)-(c) The retardance images are taken such that the boxed region has a local phase retardation around -120°, 0°, 120°. (d) The phase gradient image of the cell within the boxed region. I The retrieved QPI image of the NIH3T3 cell. (f)-(h) The retardance images of the PMMA calibration sample. (i) The phase gradient image of the edge of the 110-nm-thick PMMA thin film. (j) The QPI image of the PMMA sample. (Inset) Cross section of the QPI along dashed line.

10. Reference

1. J.E. Greivenkamp, Generalized data reduction for heterodyne interferometry. Opt. Eng. **23**, 234350 (1984).
2. W.H. Southwell, Wave-front estimation from wave-front slope measurements. J. Opt. Soc. Am. **70**, 998-1006 (1980).
3. V. Blondel, S.P. Boyd and H. Kimura Recent advances in learning and control. (Springer, 2008).
4. M.C. Grant and S.P. Boyd in Recent advances in learning and control 95-110 (Springer, 2008).